Advances in Wave-Plasma Modelling in ECR Thrusters

A. Sánchez-Villar, M. Merino
Equipo de Propulsión Espacial y Plasmas, Universidad Carlos III de Madrid, Leganés, Spain
alvaro.sanchez.villar@uc3m.es.

KEYWORDS:

ECRT, EM waves in plasma, MFEM.

ABSTRACT:

This paper presents the development status of the simulation tool THaMES (Time-Harmonic Maxwell Equations Solver) that aims to reproduce the electromagnetic (EM) wave propagation inside an ECR plasma thruster to study the ECR resonance absorption and wave propagation. THaMES allows the use of a planar domain filled with arbitrary cold magnetized inhomogeneous plasmas, specifying parameters such as the electron plasma density, the applied magnetic field or the effective collisional rate. The simulation relies on MFEM discretization library.

1. INTRODUCTION

The Electron Cyclotron Resonance thruster (ECRT) [1, 2] can be included in the electrodeless plasma thrusters class together with Helicon Plasma Thruster (HPT) [3–5]. This new generation of thrusters aims to overcome some of the issues of classic electric propulsion alternatives as ion thrusters or Hall effect thrusters. Not only the absence of the electrodes would allow increasing thruster lifetimes, but also this combined with the lack of need of neutralizer, would in principle simplify both thruster and power-processing unit designs. Furthermore these thrusters are expected to yield high thrust densities, to allow for ample throteability, and to simplify scaling to low and high powers.

Understanding the wave-plasma interaction is a crucial task of high complexity, since this interaction results from the interplay of multiple phenomena as wave propagation, cutoffs, resonances, reflection, absorption and mode conversions. Numerically solving the wave-plasma problem brings up interesting challenges, as the anisotropy introduced by the magnetic field and by the numerical mesh affects the accuracy of the simulation. Furthermore, the ECR resonance is a thin layer where the wavelength becomes considerably smaller than in other regions of the plasma. Thus, a correct treatment of resonance regions requires very fine meshes [6].

A simulation tool THaMES of the 2D time-harmonic wave electric field in a cold, magnetized inhomoegeneous plasma is presented here. THaMES allows to solve for the EM wave propagation in a domain with plasma under different antenna excitations. The code is written in C++ language and makes use of the open-source finite element discretization library MFEM. Triangular mesh elements configuring non-structured grids are chosen for this simulation since they are optimal choice to reproduce complex geometries. Choosing non-structured against structured meshes allows to apply mesh refinement for the ECR region.

This paper presents current status of the simulation tool THaMES. In Section 2 the mathematical model used for the simulation is thoroughly detailed. The implementation of THaMEs follows rigorous validation standards through testing. A test driven development has allowed the validation of new functionalities of the code, in a sequential manner. In Section 3, THaMES validation cases performed are shown and results are discussed. Finally, in Section 4, some conclusions are withdrawn and the next milestones in the code development path are described.

2. MATHEMATICAL MODEL

Maxwell's equations for a macroscopic medium are:

$$\nabla \times \boldsymbol{E} = -\frac{\partial \boldsymbol{B}}{\partial t}, \qquad \text{(Eq. 1)}$$

$$\nabla \times \boldsymbol{H} = \frac{\partial \boldsymbol{D}}{\partial t} + \boldsymbol{j}_a, \qquad \text{(Eq. 2)}$$

$$\nabla \cdot \boldsymbol{D} = \rho, \qquad \text{(Eq. 3)}$$

$$\nabla \cdot \boldsymbol{B} = 0, \qquad \text{(Eq. 4)}$$

where $\boldsymbol{E}$ is the electric field, $\boldsymbol{D}$ is the electric displacement field, $\boldsymbol{H}$ is the magnetic field, $\boldsymbol{B}$ is the induced magnetic field, μ_0 is the magnetic permeability in vacuum, ρ is the charge density and $\boldsymbol{j}_a$ is the antenna current density. The curl of Faraday's law (Eq. 1) is

$$\nabla \times (\nabla \times \boldsymbol{E}) = -\frac{\partial}{\partial t} (\nabla \times \boldsymbol{B}) . \qquad \text{(Eq. 5)}$$

We will assume linear inhomogeneous anisotropic constitutive relation for the electric displacement field and that the permeability of the medium is that of vacuum. Thus,

$$\boldsymbol{D} = \boldsymbol{\epsilon} \boldsymbol{E}, \qquad \text{(Eq. 6)}$$

$$\boldsymbol{B} = \mu_0 \boldsymbol{H}. \qquad \text{(Eq. 7)}$$

This system of equations can be reduced to the time-harmonic Maxwell system by applying Fourier transform in time domain. We will assume time-harmonic evolution the system variables (i.e. $\boldsymbol{E}, \boldsymbol{D}, \boldsymbol{H}, \boldsymbol{B}$, and to be consistent also $\boldsymbol{j}_a$ and ρ) so that:

$$\boldsymbol{E}(\boldsymbol{x}, t) = \mathrm{Re}[\hat{\boldsymbol{E}}(\boldsymbol{x}) \exp(-i\omega t)], \qquad \text{(Eq. 8)}$$

being $\hat{\boldsymbol{E}}$ is a complex-valued vector function. This allows to analyze the propagation of electromagnetic waves at a single frequency.

As a result, the time-harmonic Maxwell system can be written as:

$$\nabla \times \left(\nabla \times \hat{\boldsymbol{E}}\right) = k_0^2 \boldsymbol{\kappa} \cdot \hat{\boldsymbol{E}} + i\omega\mu_0 \hat{\boldsymbol{j}}_a, \qquad \text{(Eq. 9)}$$

where $k_0^2 = \omega^2/c^2$. In Eq.9 the dielectric tensor $\boldsymbol{\kappa}$ comprises the information regarding the dielectric properties that affect the propagation of electromagnetic waves in it. A first approach to describe it is to use the cold, magnetized plasma dielectric tensor described in the literature [7–9], defined with respect to the direction of the magnetic field. This is obtained using the zero-temperature plasma fluid equations and including energy dissipation by an effective collisionality ν_e. This can be understood as a sort of damping and subscript e stands for effective, as this mechanism is not only due to collisions. The inclusion of the effective collisionality in the model allows to solve propagation in resonance cones and ECR resonances as was described in [6]. For a plasma with s_N species and magnetic field in the x direction, the dielectric tensor takes the form :

$$\boldsymbol{\kappa} = \begin{pmatrix} P(\boldsymbol{x},\omega) & 0 & 0 \\ 0 & S(\boldsymbol{x},\omega) & -iD(\boldsymbol{x},\omega) \\ 0 & iD(\boldsymbol{x},\omega) & S(\boldsymbol{x},\omega) \end{pmatrix} \qquad \text{(Eq. 10)}$$

where S, D, P are defined as :

$$S(\boldsymbol{x},\omega) = \tfrac{1}{2}\left(R(\boldsymbol{x},\omega) + L(\boldsymbol{x},\omega)\right) \qquad \text{(Eq. 11)}$$

$$D(\boldsymbol{x},\omega) = \tfrac{1}{2}\left(R(\boldsymbol{x},\omega) - L(\boldsymbol{x},\omega)\right) \qquad \text{(Eq. 12)}$$

$$L(\boldsymbol{x},\omega) = 1 - \sum_s^{s_N} \frac{{\omega_{ps}}^2(\boldsymbol{x})}{\omega\left(\omega + i\nu_e(\boldsymbol{x}) - \omega_{cs}(\boldsymbol{x})\right)}, \qquad \text{(Eq. 13)}$$

$$R(\boldsymbol{x},\omega) = 1 - \sum_s^{s_N} \frac{{\omega_{ps}}^2(\boldsymbol{x})}{\omega\left(\omega + i\nu_e(\boldsymbol{x}) + \omega_{cs}(\boldsymbol{x})\right)}, \qquad \text{(Eq. 14)}$$

$$P(\boldsymbol{x},\omega) = 1 - \sum_s^{s_N} \frac{{\omega_{ps}}^2(\boldsymbol{x})}{\omega\left(\omega + i\nu_e(\boldsymbol{x})\right)}, \qquad \text{(Eq. 15)}$$

Note that ω_{ps} and ω_{cs} are the plasma frequency and gyrofrequency respectively of species s mass m_s and density n_s so that:

$$\omega_{ps}^2 = \frac{{q_s}^2 n_s}{\epsilon_0 m_s}, \quad \text{and} \quad \omega_{cs} = \frac{q_s B_0}{m_s}, \qquad \text{(Eq. 16)}$$

where q_s is the signed charge of species s.

A preliminary analysis of this tensor with $\nu_e = 0$ and for a two-component plasma in an homogeneous media is described by the Clemmow-Mullaly-Allis (CMA) Diagram [7]. It represents the different modes in cold plasma and bounding surfaces in plasma parameter space, as resonances, cutoffs, etc, with the x axis being the ratio $(\omega_{pe} + \omega_{pe})/\omega^2$ and the y axis $|\omega_{ce}|/\omega$. Note that in this paper we will refer to regions in this diagram as specified in [7].

The dielectric tensor can be expressed locally in a magnetic nozzle by performing a simple rotation by the angle of the magnetic field lines θ:

$$\boldsymbol{\kappa}_\theta(\boldsymbol{x},\omega) = \boldsymbol{R}^t(\theta)\boldsymbol{\kappa}(\boldsymbol{x},\omega)\boldsymbol{R}(\theta) \qquad \text{(Eq. 17)}$$

Eq.9 comprises the information of the Maxwell system for the propagation of electromagnetic waves. However, although the divergence conditions are a direct consequence of it given that charge is conserved, the divergence free condition of equation Eq.9 should not be ignored in the choice of the numerical scheme applied to solve this equation. Thus, Eq.3 and Eq.4 have to be solved, or at least satisfied when solving Eq.9.

Applying the inner product of weighting functions Φ to Eq.9, integrating by parts in the domain, one finds the weak form of equation (Eq. 9) [10]:

$$\int_\Omega \left[\left(\nabla \times \hat{\boldsymbol{E}}\right) \cdot \left(\nabla \times \hat{\boldsymbol{\Phi}}^*\right) - \frac{\omega^2}{c^2}\left(\boldsymbol{\kappa}\hat{\boldsymbol{E}}\right) \cdot \hat{\boldsymbol{\Phi}}^*\right] dV + \int_{\partial\Omega} \hat{\boldsymbol{n}} \times \left(\nabla \times \hat{\boldsymbol{E}}\right) \cdot \hat{\boldsymbol{\Phi}}^* dS = i\omega\mu_0 \int_\Omega \hat{\boldsymbol{j}}_a \cdot \hat{\boldsymbol{\Phi}}^* dV, \qquad \text{(Eq. 18)}$$

where Ω is the element volume, $\partial\Omega$ is the element boundary surfaces and $\hat{n}$ is the unit normal vector to the element boundaries. In addition, $\hat{\boldsymbol{\Phi}}^*$ is the complex conjugate of smooth vector function $\hat{\boldsymbol{\Phi}}$ (the so-called weighting or test functions). Test or weighting functions $\tilde{\Phi}$ are chosen to be equal to the shape or trial functions $\tilde{E}$, following Galerkin's Finite Element Method.

Assuming planar propagation in z coordinate, Eq.18 can be solved in a planar domain (2D), with the presence of a component of the field out of the plane. Thus the electric field takes the form:

$$\boldsymbol{E} = \mathrm{Re}\left[\left(\tilde{E}_x \mathbf{1}_x + \tilde{E}_y \mathbf{1}_y + \tilde{E}_z \mathbf{1}_z\right) \exp\left(ik_z z - i\omega t\right)\right] \qquad \text{(Eq. 19)}$$

where $\tilde{\boldsymbol{E}}_()$ are complex-valued functions of x and y coordinates. Assuming planar propagation in z

	$\tilde{\boldsymbol{E}}^r_{xy}$	$\tilde{\boldsymbol{E}}^i_{xy}$	$\tilde{E}^r_z$	$\tilde{E}^i_z$
$\tilde{\boldsymbol{\Phi}}^r_{xy}$	$(\nabla\times\tilde{\boldsymbol{\Phi}}^r_{xy})\cdot(\nabla\times\tilde{\boldsymbol{E}}^r_{xy})$ $-k_0^2\left[\boldsymbol{\kappa}^r_{xy,xy}\cdot\tilde{\boldsymbol{E}}^r_{xy}\right]\cdot\tilde{\boldsymbol{\Phi}}^r_{xy}$ $+k_z^2\tilde{\boldsymbol{E}}^r_{xy}\cdot\tilde{\boldsymbol{\Phi}}^r_{xy}$	$k_0^2\left[\boldsymbol{\kappa}^i_{xy,xy}\cdot\tilde{\boldsymbol{E}}^i_{xy}\right]\cdot\tilde{\boldsymbol{\Phi}}^r_{xy}$	$-k_0^2\tilde{E}^r_z\boldsymbol{\kappa}^r_{xy,z}\cdot\tilde{\boldsymbol{\Phi}}^r_{xy}$	$-k_z\nabla\tilde{E}^i_z\tilde{\Phi}^r_{xy}$ $+k_0^2\tilde{E}^i_z\boldsymbol{\kappa}^i_{xy,z}\cdot\tilde{\boldsymbol{\Phi}}^r_{xy}$
$\tilde{\boldsymbol{\Phi}}^i_{xy}$	$-k_0^2\left[\boldsymbol{\kappa}^i_{xy,xy}\cdot\tilde{\boldsymbol{E}}^r_{xy}\right]\cdot\tilde{\boldsymbol{\Phi}}^i_{xy}$	$(\nabla\times\tilde{\boldsymbol{\Phi}}^i_{xy})\cdot(\nabla\times\tilde{\boldsymbol{E}}^i_{xy})+$ $-k_0^2\left[\boldsymbol{\kappa}^r_{xy,xy}\cdot\tilde{\boldsymbol{E}}^i_{xy}\right]\cdot\tilde{\boldsymbol{\Phi}}^i_{xy}$ $+k_z^2\tilde{\boldsymbol{E}}^i_{xy}\cdot\tilde{\boldsymbol{\Phi}}^i_{xy}$	$k_z\nabla\tilde{E}^r_z\tilde{\Phi}^i_{xy}$ $-k_0^2\tilde{E}^r_z\boldsymbol{\kappa}^i_{xy,z}\cdot\tilde{\boldsymbol{\Phi}}^i_{xy}$	$-k_0^2\tilde{E}^i_z\boldsymbol{\kappa}^r_{xy,z}\cdot\tilde{\boldsymbol{\Phi}}^i_{xy}$
$\tilde{\Phi}^r_z$	$-k_0^2\boldsymbol{\kappa}^r_{z,xy}\cdot\tilde{\boldsymbol{E}}^r_{xy}\tilde{\Phi}^r_z$	$k_z\nabla\tilde{\Phi}^r_z\tilde{\boldsymbol{E}}^i_{xy}$ $+k_0^2\tilde{\Phi}^r_z\boldsymbol{\kappa}^i_{z,xy}\cdot\tilde{\boldsymbol{E}}^i_{xy}$	$\nabla\tilde{\Phi}^r_z\cdot\nabla\tilde{E}^r_z$ $-k_0^2\kappa^r_{zz}\,\tilde{E}^r_z\tilde{\Phi}^r_z$	$k_0^2\kappa^i_{zz}\tilde{E}^i_z\tilde{\Phi}^r_z$
$\tilde{\Phi}^i_z$	$-k_z\nabla\tilde{\Phi}^i_z\tilde{\boldsymbol{E}}^r_{xy}$ $-k_0^2\tilde{\Phi}^i_z\boldsymbol{\kappa}^i_{z,xy}\cdot\tilde{\boldsymbol{E}}^r_{xy}$	$-k_0^2\boldsymbol{\kappa}^r_{z,xy}\cdot\tilde{\boldsymbol{E}}^i_{xy}\tilde{\Phi}^i_z$	$-k_0^2\kappa^i_{zz}\tilde{E}^r_z\tilde{\Phi}^i_z$	$\nabla\tilde{\Phi}^i_z\cdot\nabla\tilde{E}^i_z$ $-k_0^2\kappa^r_{zz}\,\tilde{E}^i_z\tilde{\Phi}^i_z$

Table 1: 4x4 Block system of equations splitting real and imaginary parts of in-plane and out-of-plane components of the electric field. Note that superscripts r and i correspond to the real and imaginary parts respectively.

leads to replacing $\nabla \rightarrow \bar{\nabla} + ik_z$, in which $\bar{\nabla} = (\partial/\partial x, \partial/\partial y)$. Using some vector identities[1]:

$$\nabla\times\tilde{\boldsymbol{E}} = \bar{\nabla}\times\tilde{\boldsymbol{E}}_{xy}+ik_z\mathbf{1}_z\times\tilde{\boldsymbol{E}}_{xy}+\bar{\nabla}\tilde{E}_z\times\mathbf{1}_z \quad \text{(Eq. 20)}$$

where $\tilde{\boldsymbol{E}}_{xy} = \tilde{E}_x\mathbf{1}_x + \tilde{E}_y\mathbf{1}_y$ and $\tilde{E}_z$ are respectively the *in-plane* and *out-of-plane* electric fields.

The second integral in Eq.18 represents the effect of the boundaries. For a Perfect Electric Conductor (PEC) the tangential field is zero so that $\tilde{\boldsymbol{n}}\times\tilde{\boldsymbol{E}} = 0$. In order to apply these conditions the space of test functions chosen is restricted to those that are zero at the boundary, for all $\tilde{\boldsymbol{\Phi}}$ used.

As detailed before, the electric field of the wave solution has both a real and an imaginary part. The simulation splits both parts using a block matrix system to solve independently in real and imaginary part of the wave for both in-plane and out-of-plane components (i.e. 4x4 Block matrix) as shown in Table 1. The coupling between real and imaginary parts for in plane and out of plane components respectively appears due to the imaginary part of the dielectric tensor in the wave equation, which produces a complex refractive index that couples power from real and imaginary parts. The coupling between in-plane and out-of-plane components is a result of both the components of the dielectric tensor coupling in-plane with out-of-plane and of k_z.

Eq.18 can be solved using different element types. Each scenario to be studied may require an intelligent assessment of the finite element choice, not only for simplicity in imposing boundary conditions for each problem, but also due to the mathematical properties of the basis of functions that will affect, for instance, convergence. Nédélec elements [11, 12] are chosen for both real and imaginary parts of the in-plane components. This is due to the fact that Nédelec elements represent $H(\text{curl},\Omega)$ conforming basis of functions. For order 1, Nédélec basis of functions are defined in the edges instead of the nodes, and consist of vector fields that have a continuous tangential component and a discontinuous normal component. Their curl-conforming property allows for enhanced convergence of the method when solving Maxwell equations [10]. The reason relies in the fact that basis of functions of nodal elements in $H^1(\Omega)$ belong to a wider space in $\mathbb{R}^2$ than that of the Nédélec basis of functions. Thus, the method can in some cases converge to spurious solutions which are not satisfying Eq.3.

As the simulation tool aims to reproduce the out of plane component (being in planar or axisymmetric case), this new component cannot be included using Nédélec just increasing the space in Nédélec, as it would require increase the dimensions of the solution to $\mathbb{R}^3$ which is undesired. Instead, we will use Nédélec $H(curl,\Omega)$ elements for the in-plane $\tilde{E}$ vector components, and for the component out of plane, nodal $H^1(\Omega)$ elements are chosen.

Nédélec elements of order one, generate one degree of freedom per edge in the mesh and per vector field. For triangular cells, there are three degrees of

[1] $\nabla\times(f\boldsymbol{A}) = f\nabla\times\boldsymbol{A}+\nabla f\times\boldsymbol{A}$ and $\nabla(fg) = f\nabla g + g\nabla f$

freedom for the real and imaginary parts of the electric field in the plane. In the case of the nodal $H^1(\Omega)$ elements used for the out-of-plane component, the number of degrees of freedom goes as number of scalar functions used at the node times the number of nodes in the mesh. Note that the order of the element does not scale linearly with the number of degrees of freedom per element. For instance for Nédélec elements of order 1 the number degrees of freedom is 3, for order 2 is 8 (6 on the faces and 2 inside the triangle) and for order 3 is 15 (9 on the faces and 6 inside the cell).

After having chosen the elements and the test functions, given a mesh, the bilinear and linear integrations are defined and can be computed by MFEM. These return the coefficients of the linear system matrix in which the number of degrees of freedom depends on the finite elements type used, the boundary conditions imposed and the mesh.

The resulting problem is a linear system $\boldsymbol{A} \cdot \boldsymbol{x} = \boldsymbol{b}$, where $\boldsymbol{A}$ is a sparse matrix composed of block matrices. The solution of linear systems can be either performed by iterative algorithms or by direct solvers. As mentioned before, the linear system to be solver is described by a block sparse matrix. This matrix is not *symmetric positive definite* (s.p.d). This results from the splitting of real and imaginary parts of the vector fields.

MFEM provides different alternatives to solver linear systems in serial. However, most iterative solvers available as the Jacobi, the Gauss-Seidel (GS), Preconditioned-Conjugated-Gradient (PCG) or the Minimum Residuals (MINRES) are methods symmetric. In the case of direct solvers MFEM has multiple options for serial solvers. In order to use powerful serial solvers in MFEM, MFEM was precompiled to use the set of direct solvers contained SUITESPARSE libraries. Specifically the Unsymmetic MultiFrontal method Package (UMFPACK) was used.

In order to summarize, the resulting model of the complete 2D time-harmonic solution of Maxwell equations depends on the following:

- ω: angular frequency.
- k_z: wave number in z direction.
- $B_0(\boldsymbol{x})$: Magnetic intensity topologies.
- $\theta(\boldsymbol{x})$: Magnetic field angle.
- $n_e(\boldsymbol{x})$: Plasma density topology.
- $\nu_e(\boldsymbol{x})$: Effective collisionality topologies.
- $\boldsymbol{j}_a(\boldsymbol{x})$: Antenna current density profiles.
- Geometry and boundary conditions.

3. VALIDATION AND TESTING

At every stage in the code implementation, test runs were performed to check the old functionalities of the code and new tests for each milestone were designed, and run. The test design has followed the *method of manufactured solutions* generation of solutions, in which an analytical solution is fed into the equations to obtain the analytical equivalent forcing function. The numerical solution of the simulation due to this forcing function is compared to the exact analytical solution. The choice of the analytical solution has to be compliant with the boundary conditions. For instance, in case of imposing PEC boundary conditions, the field at the boundary should be normal. Thus the amplitude of each component of the solutions are set as follows: at $y = 0\text{m}$ and $y = H$, $\tilde{E}_x = \tilde{E}_z = 0\text{V/m}$; at $x = 0\text{m}$ and $x = L$, $\tilde{E}_y = \tilde{E}_z = 0\text{V/m}$. The test domain is a 2D rectangle of height (along y) $H = 2\text{m}$ and length (along x) $L = 5\text{m}$.

Figure 1 shows the amplitude and phase of the analytical solution which the test aims to reproduce. All tests are performed with the following manufactured solution:

$$\tilde{\boldsymbol{E}}^{an} = \begin{bmatrix} \sin(k_1 y) + i\sin(k_2 y) \\ \sin(k_1 x) + i\sin(k_2 x) \\ \sin(k_3 x)\sin(k_3 y) + i\sin(k_4 x)\sin(k_4 y) \end{bmatrix} \quad \text{(Eq. 21)}$$

For each scenario, the test forcing functions are computed from Eq.21 and Eq.9. For the sake of simplicity wave numbers k_1, k_2, k_3, k_4 are set fixed for all test cases as shown in Figure 1. The difference between both induces a non-zero phase topology as shown in the figure.

Passing several test cases is considered as milestones for the code development process, each of them having different sets of simulation parameters. Case **1** shows the simplest simulation performed. Case **1** is a case run for an unmagnetized underdense plasma (i.e. $\omega_{pe}^2/\omega^2 < 1$) that belong to CMA Region **I** [7]. Cases **2-6** are for magnetized overdense plasmas (i.e. $\omega_{pe}^2/\omega^2 > 1$ & $\omega_{ce}/\omega > 1$) corresponding to CMA Region **VIII**. The latter region is characteristic for ECR plasmas. Case **2** reproduces an overdense magnetized homogeneous plasma slab. The inclusion of a magnetic field intensity generates anisotropy in the media and couples the different different components of the electric field as shown in Eq.10. Case **3** includes a out-of-plane wave number. Case **4** increases by a factor of 3 the magnetic field intensity with respect to Case **3**. Case **5** increases the effective collisionality by one order of magnitude with respect to Case **4**. Case **6** takes Case **5** and includes inhomogeneous plasma density with quadratic profile in y axis, with maximum at $y = 0\text{m}$, and zero at $y = H$.

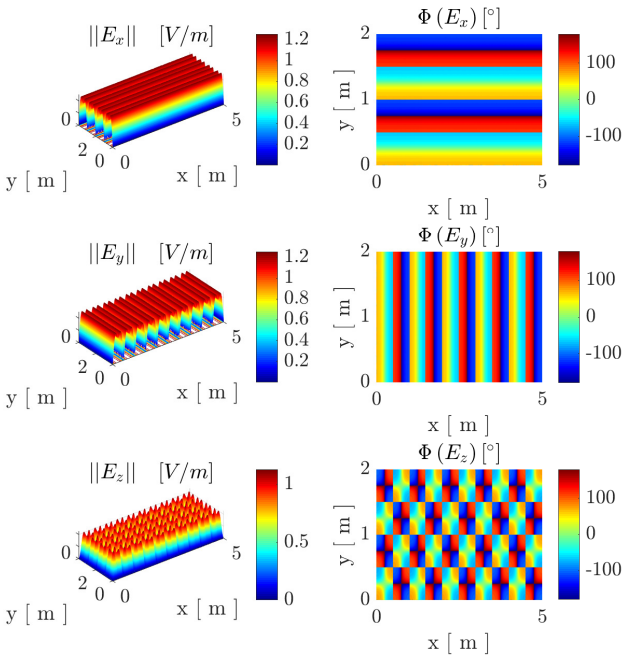

Figure 1: Manufactured solution for validation of THaMES; $k_1 = 2\pi$, $k_2 = 4\pi$, $k_3 = 2\pi$, $k_4 = 4\pi$. On the left the magnitudes of each component of the analytical electric field. On the right the phase of the complex fields $\tilde{E}_x$, $\tilde{E}_y$ and $\tilde{E}_z$.

Simulation parameters as plasma density and magnetic field intensity have been chosen to resemble those of ECRA [13]. The different case scenarios are

1. Unmagnetized underdense plasma slab ($B = 0.0\text{T}$, $n = n_0 = 5 \times 10^{16}[\text{m}^{-3}]$, $k_z = 0\text{m}^{-1}$, $\nu_e/\omega = 0.01$).
2. Magnetized overdense plasma slab ($B = B_0 = \mathbf{0.1}\text{T}$, $n = n_0 = \mathbf{2 \times 10^{17}}[\text{m}^{-3}]$, $k_z = 0\text{m}^{-1}$, $\nu_e/\omega = 0.01$).
3. Increasing k_z ($B = B_0 = 0.1\text{T}$, $n = n_0 = 2 \times 10^{17}[\text{m}^{-3}]$, $k_z = \mathbf{100}\text{m}^{-1}$, $\nu_e/\omega = 0.01$).
4. Increasing B_0 ($B = B_0 = \mathbf{0.3}\text{T}$, $n = n_0 = 2 \times 10^{17}[\text{m}^{-3}]$, $k_z = \mathbf{10}\text{m}^{-1}$, $\nu_e/\omega = 0.01$).
5. Increasing ν_e/ω ($B = B_0 = 0.3\text{T}$, $n = n_0 = 2 \times 10^{17}[\text{m}^{-3}]$, $k_z = 10\text{m}^{-1}$, $\nu_e/\omega = \mathbf{0.1}$).
6. Including inhomogeneous plasma density ($B = B_0 = 0.1\text{T}$, $n(y) = \mathbf{2 \times 10^{17}(1 - (y/H)^2)}[\text{m}^{-3}]$, $k_z = 10\text{m}^{-1}$, $\nu_e/\omega = 0.1$).

The results of the convergence analysis, and computational time of each simulation are shown in Table 2. L^2-norm error values for in-plane and out-of-plane components of the electric field are shown. The computational time expense t_{comp} is shown, together with the analysis of mesh refinement on the accuracy of the numerical solution.

First of all it can be noticed that the totality of test runs converge to the analytical solution with mesh refinement. Case **1** is shown to converge the fastest and the best of all cases. Case **2** convergence is considerably worse than that of Case **1** as can be seen in Table 2 for both in-plane and out-of-plane solutions. The effect on the computational time is increasing it by almost 50%. This is due to the fact that the solver needs to deal with a linear system whose matrix $\boldsymbol{A}$ has more non-zero coefficients per row.

Comparing convergence of Case **3** with Case **2** shows that both convergence and computational time are barely affected. Case **4** convergence compared to Case **2** is slightly worse for the former, suggesting that the magnetic field has higher impact on convergence than k_z.

Comparing Case **5** with Case **4**, it can be noticed increasing the collisionality results in improving the convergence. In Case **6** the convergence is similar but slightly worse to that of the homogeneous case (i.e. Case **5**).

Concerning t_c, it can be noticed that the test routines take similar time to run. Furthermore, the time expense increases with the number of cells as it could be expected from the increased size of the variables that the code has to deal with. Apart from that the changes between simulations are the largest between unmagnetized and magnetized plasmas.

Memory available in the unit used for the tests revealed that the system ran out of memory when UMFPACK package of solvers had to deal with meshes composed by O(10^5) elements, giving rise to around O(10^6) degrees of freedom (d.o.f.).

4. CONCLUSIONS & FUTURE WORK

This paper has presented the simulation tool THaMES being developed at Universidad Carlos III de Madrid whose final goal is to model the EM wave propagation in ECR plasma thrusters in the context of the H2020 MINOTOR project.

The mathematical model to describe the procedure to simulate a complete 2D arbitrary cold magnetized inhomogeneous plasmas with electric field in z direction has been shown. The tool has followed a Test Driven Development, testing each new functionality and running tests to check previous ones. The convergence of the totality of tests has

Variable	N	Case 1	Case 2	Case 3	Case 4	Case 5	Case 6
$\left\|\tilde{\boldsymbol{E}}_{xy}^{num} - \tilde{\boldsymbol{E}}_{xy}^{an}\right\|$	62	2.184	$1.255 \cdot 10^{1}$	$2.217 \cdot 10^{1}$	$1.476 \cdot 10^{1}$	5.830	$1.157 \cdot 10^{1}$
	188	1.087	6.766	8.402	$1.130 \cdot 101$	3.915	8.526
	652	$2.942 \cdot 10^{-1}$	1.796	2.901	1.710	$6.606 \cdot 10^{-1}$	1.489
	1232	$1.670 \cdot 10^{-1}$	$9.561 \cdot 10^{-1}$	1.363	1.261	$4.153 \cdot 10^{-1}$	$8.393 \cdot 10^{-1}$
	3402	$6.204 \cdot 10^{-2}$	$2.786 \cdot 10^{-1}$	$3.492 \cdot 10^{-1}$	$4.745 \cdot 10^{-1}$	$1.611 \cdot 10^{-1}$	$3.266 \cdot 10^{-1}$
	7504	$2.698 \cdot 10^{-2}$	$1.153 \cdot 10^{-1}$	$1.468 \cdot 10^{-1}$	$1.990 \cdot 10^{-1}$	$6.604 \cdot 10^{-2}$	$1.283 \cdot 10^{-1}$
	16690	$1.262 \cdot 10^{-2}$	$5.102 \cdot 10^{-2}$	$5.810 \cdot 10^{-2}$	$8.969 \cdot 10^{-2}$	$3.007 \cdot 10^{-2}$	$5.171 \cdot 10^{-2}$
	29760	$6.806 \cdot 10^{-3}$	$2.842 \cdot 10^{-2}$	$3.179 \cdot 10^{-2}$	$4.429 \cdot 10^{-2}$	$1.544 \cdot 10^{-2}$	$2.467 \cdot 10^{-2}$
	66056	$3.074 \cdot 10^{-3}$	$1.282 \cdot 10^{-2}$	$1.395 \cdot 10^{-2}$	$1.971 \cdot 10^{-2}$	$6.805 \cdot 10^{-3}$	$1.017 \cdot 10^{-2}$
$\left\|\tilde{\boldsymbol{E}}_{z}^{num} - \tilde{\boldsymbol{E}}_{z}^{an}\right\|$	62	1.381	8.175	9.067	$4.851 \cdot 10^{-1}$	2.435	3.356
	188	$7.132 \cdot 10^{-1}$	4.323	4.537	5.070	2.072	2.576
	652	$1.117 \cdot 10^{-1}$	1.095	1.552	$7.653 \cdot 10^{-1}$	$4.168 \cdot 10^{-1}$	$5.069 \cdot 10^{-1}$
	1232	$5.334 \cdot 10^{-2}$	$6.063 \cdot 10^{-1}$	$7.477 \cdot 10^{-1}$	$5.446 \cdot 10^{-1}$	$2.486 \cdot 10^{-1}$	$3.004 \cdot 10^{-1}$
	3402	$1.639 \cdot 10^{-2}$	$1.744 \cdot 10^{-1}$	$1.962 \cdot 10^{-1}$	$2.292 \cdot 10^{-1}$	$1.094 \cdot 10^{-1}$	$1.262 \cdot 10^{-1}$
	7504	$5.104 \cdot 10^{-3}$	$7.539 \cdot 10^{-2}$	$8.622 \cdot 10^{-2}$	$9.773 \cdot 10^{-2}$	$4.988 \cdot 10^{-2}$	$5.702 \cdot 10^{-2}$
	16690	$1.759 \cdot 10^{-3}$	$3.273 \cdot 10^{-2}$	$3.515 \cdot 10^{-2}$	$4.560 \cdot 10^{-2}$	$2.422 \cdot 10^{-2}$	$2.651 \cdot 10^{-2}$
	29760	$7.120 \cdot 10^{-4}$	$1.853 \cdot 10^{-2}$	$1.963 \cdot 10^{-2}$	$2.303 \cdot 10^{-2}$	$1.316 \cdot 10^{-2}$	$1.403 \cdot 10^{-2}$
	66056	$2.177 \cdot 10^{-4}$	$8.371 \cdot 10^{-3}$	$8.767 \cdot 10^{-3}$	$1.030 \cdot 10^{-2}$	$5.996 \cdot 10^{-3}$	$6.328 \cdot 10^{-3}$
t_c [s]	62	0.029	0.049	0.070	0.023	0.033	0.11273
	188	0.090	0.135	0.128	0.127	0.100	0.139
	652	0.381	0.339	0.324	0.353	0.306	0.304
	1232	0.538	0.495	0.625	0.780	0.521	0.517
	3402	1.340	1.268	1.518	1.621	1.284	1.259
	7504	2.492	2.832	2.902	3.463	3.174	2.915
	16690	6.225	6.810	6.861	9.532	7.236	6.848
	29760	11.122	12.532	13.153	16.924	13.475	12.910
	66056	22.774	32.825	31.803	33.566	35.119	32.725

Table 2: Convergence and computational requirements of the simulation are run for increasing number of elements $(\mathbf{N})$ *depending on the complexity of the simulation, increasing from Case* ***(I)*** *to Case* ***(VI)****.* L^2*-norm errors between the analytical* $\hat{\boldsymbol{E}}^{an}$ *and numerical* $\hat{\boldsymbol{E}}^{num}$ *solutions are displayed in absolute value with units of* $[V/m]$*. Workstation specifications: 16Gb RAM, Intel Core™i7-6700 CPU @ 3.40GHz x 8.*

been verified and computational time shown for the different scenarios studied. Modelling magnetized plasmas has proven to be more computationally demanding than nonmagnetized as could be expected due to the increase of the non-zero elements in system sparse matrix. Increasing effective collisionality has shown to improve the convergence of the solver for these conditions. Memory limitations of the simulation in te current, low-end machine were found when dealing with problems with O(10^5) elements and around O(10^6) degrees of freedom. However for the purpose of these test runs, this issue was not hindering the results of the test, which are meant to be light in memory requirements.

As a result, we have presented a preliminary version of THaMES, a 2D Finite Elements Frequency Domain simulation tool based on MFEM C++ discretization library capable of solving Maxwell Equations in 2D plasmas using nonstructured meshes.

Future work will focus on the development of a fully axisymmetric simulation of EM wave propagation inside ECR thrusters. This modification will require to upgrade operators in the simulation. In cylindrical coordinates, assuming planar propagation in θ coordinate so that $\boldsymbol{E}\hat{(\boldsymbol{x})} = \tilde{\boldsymbol{E}}(\boldsymbol{x})\exp(im\theta)]$. Thus the curl would take a similar form to that of Eq.20:

$$\nabla \times \tilde{\boldsymbol{E}} = \bar{\nabla} \times \tilde{\boldsymbol{E}}_{rz} + \frac{im_\theta}{r}\mathbf{1}_\theta \times \tilde{\boldsymbol{E}}_{rz} + \frac{1}{r}\bar{\nabla}\left(r\tilde{E}_\theta\right) \times \mathbf{1}_\theta \quad \text{(Eq. 22)}$$

where $\tilde{\boldsymbol{E}}_{rz}$ and $\tilde{E}_\theta$ are respectively the vector of *in plane* components and the *out of plane* component of the electric field. Additionally, boundary conditions for axisymmetry will have to be specified.

Furthermore, the dielectric tensor presented here simplifies the physics in ECR plasmas considerably. The wave absorption can be both collisional and kinetic. Effects as resonance broadening and Doppler shift are not modelled here.

Resonance modelling together with a antenna configuration similar to that of the ECRA thruster [13] will be included. Different forcing functions will be tried to solve for the wave electric field generated

inside the thruster. Propagation in a magnetic nozzle configuration will be addressed. Development of perfectly matched layer (PML) boundary conditions will be performed, to simulate the operation of the device in space, and compute radiation resistance to free space of the antenna. Moreover the effects of the vacuum chamber on the EM wave propagation and fields inside the thruster will be investigated. Von Neumann analysis of different FEM schemes could be performed. Furthermore, the assessment of the rigor of the use of nodal elements for the out of plane component regarding the divergence free condition will be addressed, specially for the axisymmetric case.
Iterative solvers as the Generalized Minimal Residual Solver (GMRES) available in MFEM will be investigated, together with appropriate preconditioners.

ACKNOWLEDGEMENTS

The research leading to these results has received funding from the European Union H2020 Program under grant agreement number 730028 (Project MINOTOR).

5. REFERENCES

[1] Sercel, J. C., "Electron-cyclotron-resonance (ECR) plasma acceleration," *AIAA 19th Fluid Dynamics, Plasma Dynamics and Lasers Conference*, 1987.

[2] Jarrige, J., Elias, P.-Q., Cannat, F., and Packan, D., "Characterization of a coaxial ECR plasma thruster," *44th AIAA Plasmadynamics and Lasers Conference, San Diego*, 2013.

[3] Ahedo, E. and Navarro-Cavallé, J., "Helicon thruster plasma modeling: Two-dimensional fluid-dynamics and propulsive performances," *Physics of Plasmas*, Vol. 20, No. 4, 2013, pp. 043512.

[4] Takahashi, K., Lafleur, T., Charles, C., Alexander, P., Boswell, R., Perren, M., Laine, R., Pottinger, S., Lappas, V., Harle, T., et al., "Direct thrust measurement of a permanent magnet helicon double layer thruster," *Applied Physics Letters*, Vol. 98, No. 14, 2011, pp. 141503.

[5] Charles, C., "Plasmas for spacecraft propulsion," *Journal of Physics D: Applied Physics*, Vol. 42, 2009, pp. 163001.

[6] Merino, M., Sánchez-Villar, A., and Ahedo, E., "Wave Propagation and Absorption in ECR Plasma Thrusters," 35^{th} *International Electric Propulsion Conference*, No. IEPC-2017-105, Electric Rocket Propulsion Society, Fairview Park, OH, 2017.

[7] Stix, T. H., *Waves in plasmas*, Springer Science & Business Media, 1992.

[8] Lieberman, M. and Lichtenberg, A., *Principles of plasma discharges and materials processing*, Wiley-Blackwell, 2005.

[9] Heald, M. A. and Wharton, C. B., "Plasma diagnostics with microwaves," 1965.

[10] Monk, P., *Finite element methods for Maxwell's equations*, Oxford University Press, 2003.

[11] Nédélec, J.-C., "Mixed finite elements in $\mathbb{R}^3$," *Numerische Mathematik*, Vol. 35, No. 3, 1980, pp. 315–341.

[12] Nédélec, J.-C., "A new family of mixed finite elements in $\mathbb{R}^3$," *Numerische Mathematik*, Vol. 50, No. 1, 1986, pp. 57–81.

[13] Packan, D., Elias, P.-Q., Jarrige, J., Merino, M., Sánchez-Villar, A., Ahedo, E., Peyresoubes, G., Holste, K., Klar, P., Bekemans, M., Scalais, T., Bourguignon, E., Zurbach, S., Mares, M., Hooque, A., and Favier, P., "The MINOTOR H2020 project for ECR thruster development," 35^{th} *International Electric Propulsion Conference*, No. IEPC-2017-547, Electric Rocket Propulsion Society, Fairview Park, OH, 2017.